![The University of Osaka Institutional Knowledge Archive](OUKA logo)

The University of Osaka
Institutional Knowledge Archive

Title	Simultaneous visualization of membrane fluidity and morphology defines adhesion signatures of cancer cells
Author(s)	Matsuzaki, Takahisa; Fujii, Mai; Noro, Hayata et al.
Citation	Biophysics and Computational Biology. 2024, 121(50), p. 867
Version Type	VoR
URL	https://hdl.handle.net/11094/98577
rights	This article is licensed under a Creative Commons Attribution-NonCommercial-NoDerivatives 4.0 International License.
Note	

The University of Osaka Institutional Knowledge Archive : OUKA

https://ir.library.osaka-u.ac.jp/

The University of Osaka

PNAS

Simultaneous visualization of membrane fluidity and morphology defines adhesion signatures of cancer cells

Takahisa Matsuzaki[a,b,1] (ID), Mai Fujii[c,2], Hayata Noro[c,2], Shodai Togo[c,2], Mami Watanabe[c], Masami Suganuma[d] (ID), Shivani Sharma[e], Naritaka Kobayashi[d], Ryuzo Kawamura[c], Seiichiro Nakabayashi[c,d], and Hiroshi Y. Yoshikawa[a,1] (ID)

Affiliations are included on p. 8.

We developed an advanced optical microscope for the simultaneous visualization of membrane fluidity and morphology to define cell adhesion signatures. This microscope combines ratiometric spectral imaging of membrane fluidity and interferometric imaging of membrane morphology. As a preliminary demonstration, we simultaneously visualized the interface between a giant unilamellar vesicle (GUV) and a glass substrate at different temperatures. We identified more fluid regions of the membrane and membrane adhesion sites (conversely, low-fluidic, ordered membrane domains correlate with nonadhered regions). This microscopic system was applied to human breast cancer cell lines with different malignancies; then, we identified adhesion signature of cancer cells: 1) low-fluidic, ordered membrane domains at the cell periphery and 2) large fluidic deviation at the nonadhered region. Inhibition of the cholesterol synthesis pathway suppresses the ordered membrane domains at the cancer cell periphery; thus, high level of cholesterol supports the appearance. Furthermore, an inhibitor of the unsaturated lipid synthesis pathway suppressed the large fluidic deviation at the nonadhered region; variation of unsaturated lipids contributes to heterogeneity of the cancer membrane. Therefore, our advanced optical microscopy enables us to couple membrane physical properties with cell adhesion, leading to definition of adhesion signatures of broad cell types, not just for cancer cells, that regulate life phenomena.

Laurdan | interference reflection microscopy | cell adhesion | membrane physics

Cell adhesion is a crucial step in various life phenomena, such as development (1, 2), tissue homeostasis (3, 4), and cancer metastasis (5–8). From the standpoint of molecular biology, cell adhesion is discussed mainly in terms of mechanisms involving cell adhesion molecules (CAMs, e.g., integrins and cadherins), which can provide specific key–lock interactions between cells and their environments. To understand the mechanisms underlying cell adhesion, fluorescence imaging techniques are gold standard to visualize the localization and distribution of CAMs in living cells (9). However, by relying on fluorescence visualization of CAMs alone, the physical impact of cell membranes as a dynamic and fluidic support for CAM onto cell adhesion behavior cannot be clearly defined. In fact, several studies have recognized that the membrane fluidity of cells is a physical factor that characterizes cell adhesion. For instance, Shaeffer and Curtis reported that addition of saturated fatty acids to mouse fibroblasts accelerated cell spreading onto a substrate (10). They explained the origin of accelerating adhesion by suggesting that a low-fluidic saturated membrane might restrict the lateral migration of adhesion sites. By using supported lipid layers, Salaita et al. experimentally proved that fully saturated lipid bilayers on the substrate restrict EphA2 receptor movement in human breast cancer cells, leading to different adhesion patterns (11). Regarding other CAM families, Eich et al. reported that the addition of sphingomyelinase affects sphingomyelin levels in human monocytes, resulting in impaired cell adhesion via reducing integrin mobility (12). Based on this accumulated evidence that tuning of membrane fluidity of cell membranes controls cell adhesion, fluorescence imaging with the environment-sensitive fluorescent, lipophilic probe 6-dodecanoyl-2-dimethylaminonaphthalene (Laurdan) is a leading technique to visualize spatiotemporal distribution of membrane fluidity in single "living" cells (1). Gaus et al. further combined membrane fluidity imaging with immunofluorescence imaging for CAMs and identified low-fluidic focal adhesion domains in "fixed" cells (13). Here, cell adhesion is mediated not only by biological key–lock interactions but also by various physical interactions (e.g., electrostatic interactions and steric repulsion) (14). Such physical interaction cannot be visualized using conventional fluorescence imaging of CAMs alone. In addition, immunofluorescence staining using surfactants/multiple chromophores may cause significant changes in the cell membrane fluidity itself. Therefore, to address

Significance

Developing methodologies for evaluating structures and physical properties of living cell membranes is essential for understanding the functions of biological systems. Herein, we developed advanced optical microscopy that enables the simultaneous imaging of membrane fluidity and morphology at the cell–substrate interface by combining interferometry with ratiometric fluorescence imaging. We identified low-fluidic domains at the cell periphery and the large fluidic deviation as key adhesion signatures of breast cancer cells. Drug inhibition experiments revealed that 1) the low-fluidic domains are supported by cholesterol synthesis and 2) the high level of unsaturated lipid synthesis contributes to the large fluidic deviation indicating lipid compositional heterogeneity in the cancer cell membrane. Collectively, adhesion signature of the cell membrane can be a physical hallmark of cancer malignancy and lipid heterogeneity.

how cells regulate their adhesion through cell membranes, technological developments are required to determine the correlation between membrane fluidity and the adhesion of living cells.

In this study, to simultaneously evaluate correlation between membrane fluidity and morphology at cell adhesion interfaces, we developed an advanced optical microscope combining two different methodologies (Fig. 1). First, we adopted ratiometric fluorescence microscopy using a environment-sensitive fluorescent, lipophilic probe, Laurdan, to evaluate cell membrane fluidity. The Laurdan probe is easily incorporated into the cell membrane (Fig. 1, *Left*) and fluoresces depending on the fluidity of the cell membrane (1, 5, 15, 16). We detected fluorescence signals with two different GaAsP detectors: Ch1(λ_{em} = 420 to 460 nm $I_{420-460}$) and Ch2 (λ_{em} = 474 to 515 nm, $I_{474-515}$) through two-photon excitation, which can achieve the fine spatial resolution at the cell–substrate interfaces. The fluorescence signals were then processed to obtain the generalized polarization (GP), which is a physical measure of the membrane fluidity of the cells, according to Eq. **1** (1, 15, 16):

$$GP = \frac{I_{420-460} - G \times I_{474-515}}{I_{420-460} + G \times I_{474-515}}. \qquad [1]$$

The *G* value is the calibration factor, as defined in Eq. **2**:

$$G = \frac{GP_{meas} + 1}{GP_{meas} - 1} \div \frac{GP_{ref} + 1}{GP_{ref} - 1}. \qquad [2]$$

The G value was calculated using the Laurdan probe measured the GP in DMSO (GP_{meas}) and a previously reported reference GP (GP_{ref} = 0.207). Based on this analysis, we obtained GP images and the corresponding histograms of the lipid membrane (*SI Appendix*, Fig. S1). Second, we introduced interference reflection microscopy (IRM), a powerful label-free technique for visualizing membrane morphology at cell–substrate interfaces. We used a continuous wave laser (λ = 561 nm) and obtained interference signals (I) between the reflected lights from the liquid–substrate (I_1) and liquid–cell membrane (I_2) interfaces (Fig. 1, *Left*). The optimal combination of optical mirrors and filters enabled the collection of interference signals at the PMT detector (Ch3) (Fig. 1, *Right*). Assuming quasi-normal incidence, the interference intensity, *I*, can generally be written as Eq. **3**:

$$I = I_1 + I_2 + 2\sqrt{I_1 I_2}\cos(4\pi nh/\lambda + \pi). \qquad [3]$$

The practical equation converting *I* to the cell membrane–substrate height (*h*) at sub-nm axial resolution (17) was determined as shown in Eq. **4**:

$$\frac{2I - (I_{max} + I_{max})}{-(I_{max} - I_{max})} = \cos\left(\frac{4\pi nh}{\lambda}\right), \qquad [4]$$

where *n* is the refractive index of the medium, and I_{max} and I_{min} are the maximum and minimum intensities of the interference fringes, respectively. I_{max} was carefully determined from the interference fringes originating at the bottom of the cells, as described in our previous study (18). Based on such optical optimization for the simultaneous collection of fluorescence and interference signals, we can evaluate GP and *h* as physical measures that reflect membrane fluidity and morphology at cell–substrate interfaces. In this study, to validate our combination microscope for simultaneous evaluation of membrane fluidity and cell adhesion, we visualized the interface between a giant unilamellar vesicle (GUV) and a glass substrate at different temperatures. We next applied this microscopy system to evaluate the adhesion of human breast cancer cell lines (malignant: MCF7 and nonmalignant: MCF10A) to identify adhesion signatures that reflect cancer malignancy. Furthermore, to identify the molecular origins that support adhesion signatures, we treated cells with specific drug inhibitors for certain lipid biosynthetic pathways.

Results

Adhesion Signature of a GUV. Fig. 2*A* shows the GP, IRM, and reconstructed height images of a GUV adhered to a substrate (at 37 °C). The positively charged substrate attracted the negative phosphate group of 1,2-dioleoyl-sn-glycero-3-phosphocholine (DOPC) lipids and supported the adhesion of GUV. We calculated GP using Eq. **1** and detected higher GP domains at the GUV periphery (white arrow, *GP* = 0.17 ± 0.46) compared to the center region (GP = –0.08 ± 0.45). Higher GP domains (i.e., low-fluidic, ordered membrane domains) were clearly overlapped with the region showing brighter interference signals in the corresponding IRM image (white arrow) than in the darker region of the center. Using Eq. **4**, regions with the brighter interference signals were identified as nonadhesion regions (40 ≤ *h* ≤ 80 nm). In contrast, the lower GP domains (high-fluidic, disordered membrane domains) were mainly located in the central region, with darker interference signals (yellow dotted line). Using Eq. **4**, the regions with darker interference signals were identified as adhered regions (0 ≤ *h* ≤ 40 nm).
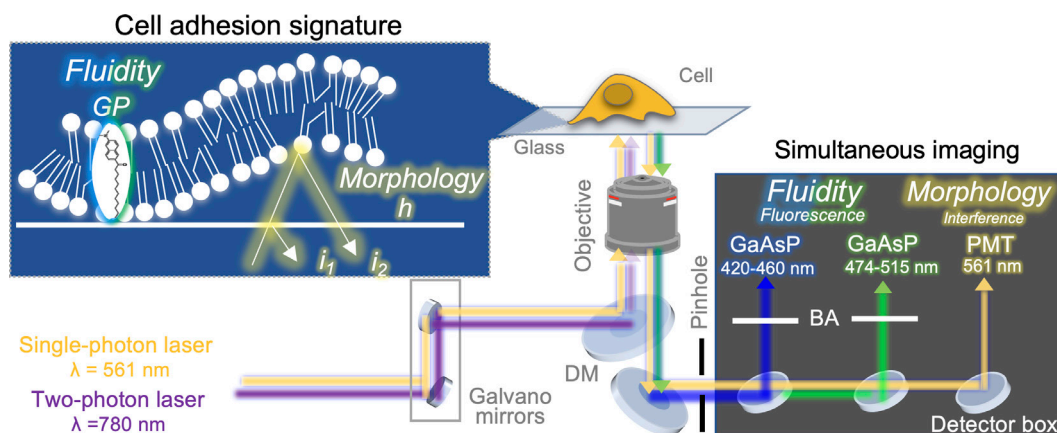

Fig. 1. Optical setup for simultaneous visualization of membrane fluidity and morphology of cell adhesion. Fluorescence signals from Laurdan (femtosecond laser source for two-photon imaging, λ = 780 nm) were collected in GaAsP channels in the detector box. Fluorescence at the wavelength range of 420 to 460 nm (Ch1) and 474 to 515 nm (Ch2) was detected separately using different combinations of dichroic mirror (DM) and barrier filters (BA). To obtain interference signals (CW laser, λ = 561 nm) at PMT (Ch3), reflection from the interface of the medium cell membrane–medium (I_1) and the medium substrate-medium (I_2) was detected.
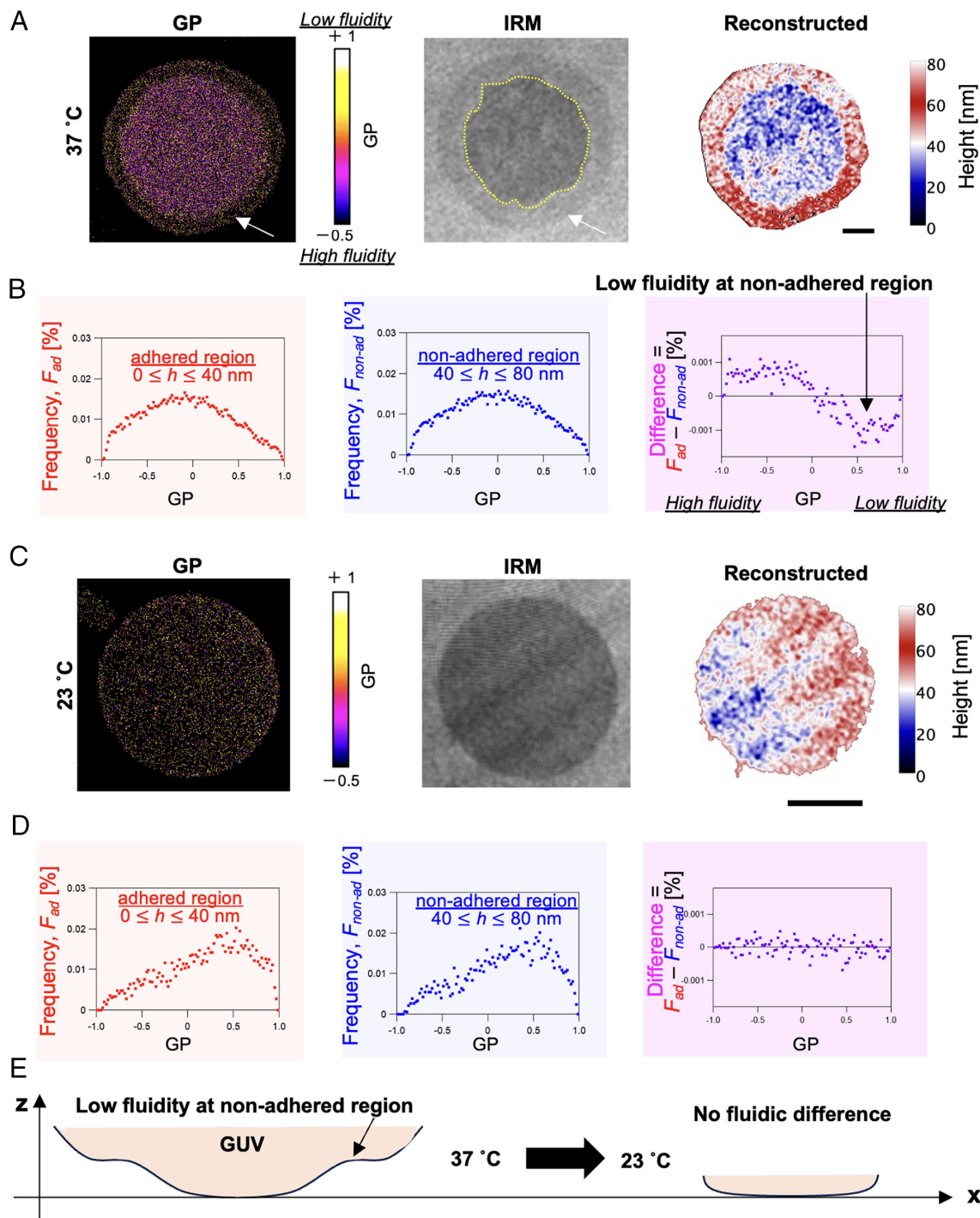
Fig. 2. Low-fluidic, nonadhered domains at the periphery define the adhesion signature of a GUV. (*A*) GP, IRM, and reconstructed height images of GUV at 37 °C. Higher GP domains were clearly segregated by brighter interference signals (yellow dots lines), and white arrows show high GP domains (low-fluidic, ordered membrane domains at nonadhered regions 40 < *h* < 80 nm). (*B*) Corresponding fluidic difference ($F_{ad} − F_{non-ad}$) between GP histograms of nonadhered and adhered regions (0 < *h* < 40 nm). Here, the frequency of histograms for the adhered and nonadhered regions was defined as F_{ad} and F_{non-ad}, respectively. (*C*) GP and IRM reconstructed height images of GUV at 23 °C and the (*D*) corresponding fluidic difference between GP histograms of nonadhered and adhered regions. Here, fluidic lipids such as 1,2-dioleoyl-sn-glycero-3-phosphocholine (DOPC) were used. The glass surface was modified with the positively charged molecule via silane coupling, and its electrostatic interaction promoted adhesion (*Materials and Methods*). (The scale bar represents 10 μm.) (*E*) Schematic summary of the adhesion signatures of GUVs. Low membrane fluidity at nonadhered domains at the cell periphery supported by the temperature elevation.

The obtained results visibly highlight low-fluidic, ordered membrane at the periphery as an adhesion signature of GUV.

To quantitatively highlight the fluidic differences between the nonadhered and adhered regions, the GP histogram of the nonadhered region (F_{non-ad}, blue) was subtracted from that of the adhered regions (F_{ad}, red) (Fig. 2*B*). Here, the GP histograms were obtained from the corresponding GP images (analysis protocol, *SI Appendix,* Fig. S2). The calculated fluidic difference ($F_{ad} − F_{non-ad}$, purple)

showed a double peak (at GP approximately –0.5, +0.5). The graph indicates that the GP histogram at the nonadhered region had a higher GP (low-fluidic membrane at the nonadhered region) compared with the adhered region. We systematically investigated the adhesion of the GUV at a lower temperature (23 °C) (Fig. 2*C*). Low-fluidic membrane domains at the GUV periphery were not detected at 23 °C. Instead, the GP distribution (~ 0.197 ± 0.006) was almost similar in the nonadhered/adhering regions in the

center. We also confirmed that calculated fluidic difference did not show peaks (Fig. 2D, purple), indicating that there is no fluidic difference between the adhered and nonadhered regions. These obtained results highlight that our advanced optical microscopy enables us to simultaneously visualize membrane fluidity and morphology. In addition, we sensitively detected unique adhesion signatures of GUV as low-fluidic, ordered membrane domains at the nonadhered region (Fig. 2E) that is supported by the temperature elevation.

Adhesion Signatures of Human Breast Malignant Cells. In the next step, to assess the applicability of our advanced optical microscopy to "living" cells, we simultaneously obtained GP, IRM, and reconstructed height images of human breast cancer cell lines (MCF7 and MCF10A) adhered to a fibronectin-coated substrate (Fig. 3A). Interestingly, GP images of malignant MCF7 cells showed low-fluidic, more ordered membrane domains (higher GP ~ 0.5) at the cell periphery compared to those in the central region (GP ~ 0.3) (*Top* panel, white arrow). It should
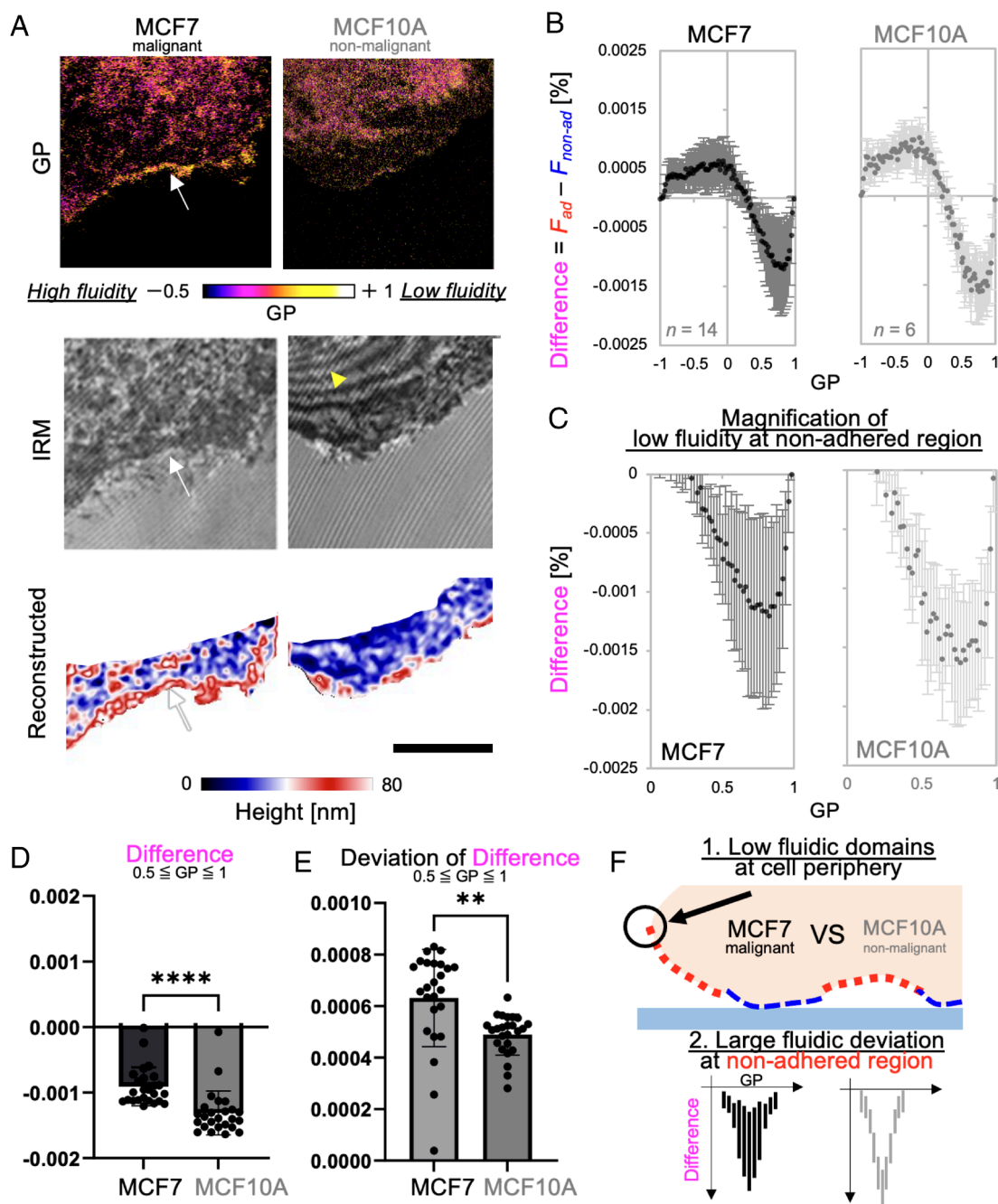

Fig. 3. Adhesion signatures of breast human malignant cells are lowly fluidic, nonadhered domains at the cell periphery and have a large SD. (A) GP, IRM, and reconstructed height images of nonmalignant (MCF10A) and malignant (MCF7) human breast cancer cells. (The scale bar represents 10 μm.) White arrows indicate the cell periphery, where low-fluidic, nonadhered domains are present. A yellow arrowhead indicates scattering and/or reflection signals from untargeted cell components (e.g., cell nuclei, upper membrane). The region (within 5 μm from the cell periphery) was clipped for the height reconstruction. (B) Corresponding fluidic difference and (C) its magnification between the nonadhered/adhered regions for cells. The error bar represents the SD of cells (Mean ± SD), and each number of analyzed cells (*n*) is displayed on the histograms. (D) Statistical analysis of "difference" and (E) SD of "difference" at 0.5 ≦ GP ≦ 1. Each dot represents the "difference" and the SD of the "difference" of each GP value. An unpaired *t* test was performed for the graphs (*P < 0.05, **P < 0.01, ***P < 0.001, and ****P < 0.0001). (F) Schematic summary of the adhesion signatures of cells. Cross-sectional view of a cell adhered to the substrate is displayed. 1) Low-fluidic visible domains at the cell periphery and 2) large deviation of low-fluidic, ordered membrane domains at the nonadhered region are key signatures for malignant cancer cells.

be noted that such low-fluidic domains were less prominent for nonmalignant MCF10A cells (another dataset also confirms such trends in *SI Appendix*, Fig. S4C). Here, the domains were clearly overlapped with the region showing brighter interference signals in the corresponding IRM image (*Middle* panel, white arrow). Here, before reconstructing height images, the interferometric signals in a center region of cells tend to be disturbed by scattering and/or reflection signals from untargeted cell components (e.g., cell nuclei, upper membrane) (*Middle*, yellow arrowhead). Thus, the region that is close to a cell margin (within 5 µm from the cell edge) was clipped for further analysis of membrane fluidity. Reconstructed height images indicate that low-fluidic domains were typically located at nonadhered regions ($40 \leq h \leq 80$ nm) (*Bottom*, white arrow). In contrast, high-fluidic, disordered membrane domains were found at adhered regions ($0 \leq h \leq 40$ nm). Such a short-range interaction for cells is supported by the key–lock interaction [i.e., integrin–fibronectin complex and other physically attractive forces (14)]. Thus, our advanced optical microscopy detected adhesion signatures of malignant cells as low-fluidic, ordered membrane domains at the cell periphery (Fig. 3 *F*, *Top*).

To quantitatively highlight the fluidic difference between the nonadhered and adhered regions, we calculated the fluidic difference ($F_{ad} - F_{non-ad}$) according to the same analytical procedure used for the GUVs. Both graphs for MCF7 and MCF10A cells provided positive and negative peaks at GP approximately –0.3 and +0.8, respectively (Fig. 3B). The result indicates that GP histogram at the nonadhered region had a higher GP (low-fluidic membrane domains at the nonadhered region). From the magnification of such domains ($0 <$ GP < 1), we detected less difference and 1.7-times larger SD for MCF7 cells (-0.0012 ± 0.00082 at GP $= +0.8$) than MCF10A cells (-0.0016 ± 0.00048 at GP $= +0.8$) (Fig. 3C). We performed statistical *t* test for the GP histograms in Fig. 3C to clarify whether there is a significant fluidic difference between MCF7 and MCF10A. Statistical analysis for fluidic difference graphs confirms that there is smaller values of "difference" (Fig. 3D) with a larger SD (Fig. 3E) for MCF7 cells. Here, the statistical analysis was performed for the GP range including negative peak ($0.5 <$ GP < 1), and such trends were not apparent at wider GP range ($-1 <$ GP < 1, *SI Appendix*, Fig. S4 *A* and *B*, *Top*). Even though low-fluidic, ordered membrane domains at nonadhered regions are a common membrane feature for GUVs and living cells. We sensitively detected large fluidic deviation of the membrane at the nonadhered region as an additional adhesion signature for cancer cells (Fig. 3 *F*, *Bottom*).

Biomolecular Origins That Influence Adhesion Signatures of Malignant Cells. Taking the above results together, we first detected cancer-specific adhesion signatures: 1) low-fluidic, ordered membrane domains at the cell periphery and 2) large fluidic deviation at the nonadhered region (Fig. 3F). To unshed the biomolecular origins of such adhesion signatures, as a first step, one of key fluidity determinants, a cholesterol biosynthetic pathway was assessed. A previous cohort study showed that 3-hydroxy-3-methylglutaryl coenzyme A reductase (HMGCR) was highly expressed in breast cancer patients, and its specific inhibition contributes to cancer survival (19). Therefore, we first treated MCF7 cells with a specific HMGCR inhibitor (lovastatin). Fig. 4 *A* (*Left* panels) shows GP, IRM, and reconstructed height images after treatment of 1 nM of lovastatin. A GP image indicates that the low-fluidic, ordered membrane domains at the cell periphery were significantly suppressed (white arrow). From the IRM image, we detected brighter interference signals at the cell periphery. From the reconstructed height images, we assigned the location is nonadhered regions (white arrow). Thus, the results indicate

that cholesterol levels contribute low-fluidic, ordered membrane domains at the cell periphery (Fig. 4 *F*, *Top*).

Calculated fluidic difference ($F_{ad} - F_{non-ad}$) did not show peaks that was observed for control (Fig. 4 *B*, *Middle*). The results indicate that lovastatin reduces the fluidic difference between the adhered and nonadhered regions. The magnified histgram around low-fluidic, ordered domains at nonadhered regions ($0 \leqq$ GP $\leqq 1$) also shows smaller values of "difference" with comparable large SD (Fig. 4 *C*, *Middle*). From the statistical analysis, lovastatin treatment leads less "difference" (Fig. 4D) with a comparable SD (Fig. 3E) for MCF7 cells. Here, the statistical analysis was performed for the GP range including negative peak ($0.5 <$ GP < 1), and such trends were not apparent at wider GP range ($-1 <$ GP < 1, *SI Appendix*, Fig. S5 *A* and *B*, *Top*). These results indicate that cholesterol levels surely support low-fluidic, ordered membrane domains at nonadhered region, and do not influence to large fluidic deviation that is another adhesion signature of malignant cells.

To assess other fluidity determinants that affect the large fluidic deviation of malignant cells, we next focus on unsaturated lipid biosynthetic pathways. Angelucci et al. identified stearoyl-CoA desaturase 1 (SCD1), a prominent driver of breast cancer progression (20) and its specific inhibition suppressed adhesion of cancer cells. Thus, we treated malignant MCF7 cells with a specific inhibitor of SCD1 (CAY10566), Fig. 4 *A* (*Right* panels) shows GP, IRM, and the reconstructed height images after treatment with 1 nM of CAY10566. A GP image indicates that CAY 10566 treatment does not influence the disappearance of the ordered membrane domains at the cell periphery (white arrow). In contrast to MCF7 (without treatment) showing inhomogeneous adhesion (Fig. 3 *A*, *Left*), MCF 7 that was treated with CAY10566 led homogeneous gray interference intensity (yellow arrow) in IRM image, and the location is attributed to nonadhered region in reconstructed height image. The results proposed that unsaturated lipid levels may contribute to reducing the heterogenic distribution of the malignant cell membrane.

To confirm such trends, we calculated fluidic difference graphs. As seen in the control graph, the results showed positive and negative peaks appeared at the same GP at approximately –0.3 and +0.8, respectively (Fig. 4 *B*, *Right*). From the magnification of low-fluidic, ordered domains at nonadhered regions show larger negative peak difference with smaller SD (Fig. 4 *C*, *Right*). Statistical analysis also indicates that CAY10566 treatment leads larger difference (Fig. 4D) with smaller SD (Fig. 4E). Here, the statistical analysis was performed for the GP range including negative peak ($0.5 <$ GP < 1). Larger negative peak difference was less apparent at wider GP range ($-1 <$ GP < 1, *SI Appendix*, Fig. S5 *A*, *Top*); thus, the statistical analysis should be performed for the GP range including peak (i.e., $0.5 <$ GP < 1). The results indicate that an unsaturated lipid synthesis pathway increased lipids levels with different saturation, leading to fluidic deviation at the nonadhered region for malignant cells (Fig. 4 *F*, *Bottom*).

Combining these results, we define the molecular origins of adhesion signature of malignant cancer cells in Fig. 4*F*: (1) ordered membrane domains at the cell periphery are supported by the high level of cholesterol, and (2) large fluidic deviation at the nonadhered region is high level of unsaturated lipid synthesis.

Discussion

In this study, we developed an advanced optical microscope to simultaneously image the environment-sensitive fluorescent, lipophilic probe Laurdan and conduct IRM to measure the height of the "living" cell membrane above the substrate (Fig. 1). This study
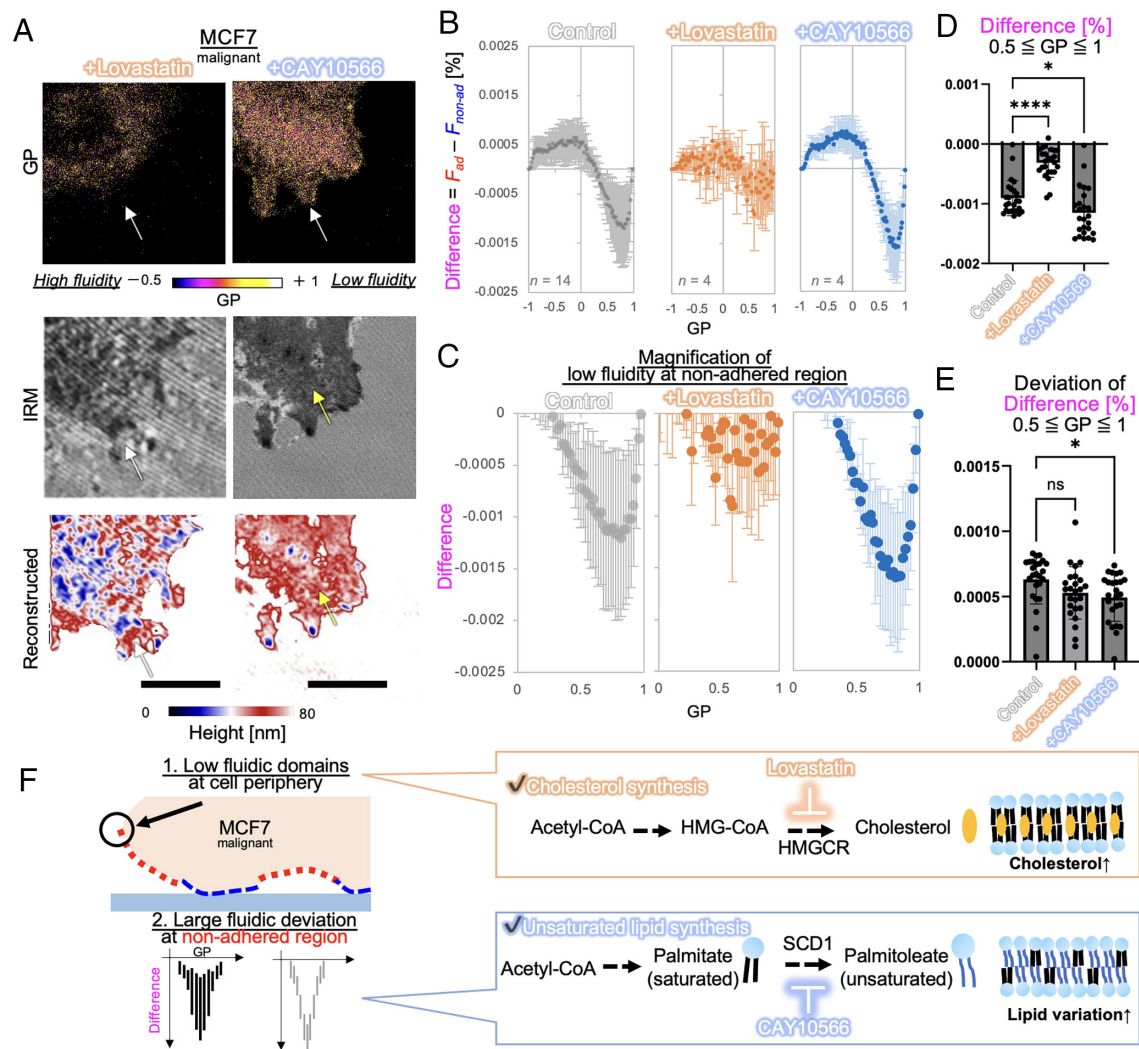
Fig. 4. Adhesion signatures of breast human malignant cells are supported by high levels of cholesterol synthesis and lipid desaturation. (*A*) GP, IRM, and reconstructed height images of malignant cell line MCF7 after the mild treatment with lovastatin (inhibitor of HMGCR and of cholesterol biosynthesis). White arrows indicate the cell periphery. Yellow arrows indicate the homogenous interreference patterns at the nonadhered region. (*B*) Corresponding mean fluidic "difference" between the nonadhered/adhered regions for cells and (*C*) its magnification at $0 \leqq GP \leqq 1$. The error bar represents the SD of cells (Mean ± SD), and each number of analyzed cells (*n*) is displayed on the histograms. To support the readers' understanding, Fig. 3 *B* and *C* is redisplayed as a control graph. Statistical analysis of (*D*) "difference" and (*E*) SD of "difference" at $0.5 \leqq GP \leqq 1$. Each dot represents the "difference" and the SD of the "difference" of each GP value. One-way ANOVA was performed for the graphs (*$P < 0.05$, **$P < 0.01$, ***$P < 0.001$, and ****$P < 0.0001$). (*F*) Schematic summary of the adhesion signatures of malignant cells and their molecular origins. A cross-sectional view of a cell adhered to the substrate is displayed. Low membrane fluidity at nonadhered domains is supported by the cholesterol synthetic pathway, and its large deviation is contributed by the unsaturated lipid synthesis pathway. Only a representative intermediate metabolite is displayed.

aims to understand the coupling of membrane physical property and cell adhesion, overcoming some of the potential shortcomings of previous methods. Based on the fluidic difference analysis between the adhered/nonadhered membrane region, one clear finding is a correlation between more fluid regions of the membrane and membrane adhesion sites (conversely, low-fluidic, ordered membrane domains correlate to nonadhered regions). This correlation of adhesion and fluidity is commonly observed in single-component lipid GUVs (Fig. 2*B*), as well as in human breast cancer cells (Fig. 3*B*) and mouse melanoma cells (*SI Appendix,* Fig. S3*B*). Therefore, our advanced optical microscope has the advantage to extract such correlation of "living" cell adhesion and fluidity as a general biophysical feature of membranes.

We also have a particular focus on understanding possible differences in these properties between malignant and nonmalignant cell lines. Our advanced optical microscopy clearly revealed that low-fluidic, ordered membrane domains at the cell periphery were more prominent for malignant cancer cells (Fig. 3*A*, white arrows). Analysis of fluidic difference between adhered/nonadhered regions

detected a large distribution of the low-fluidic, ordered membrane domains correlated to nonadhered regions, especially for malignant cells (Fig. 3 *C* and *E*). An inhibitor treatment for the cholesterol synthesis pathway suppressed such large distribution, leading to the disappearance of low-fluidic, ordered membrane domains at the cell periphery (Fig. 4*A*, white arrow). The obtained results indicate that the cholesterol accumulates in nonadhered regions and supports the low-fluidic, ordered membrane regions at the cell periphery. Furthermore, an inhibitor treatment for the unsaturated lipid synthesis pathway suppressed large distribution of low-fluidic, ordered membrane regions at the nonadhered regions (Fig. 4 *C, Right*). The results indicate that the mono-/polyunsaturated lipid leads to the large distribution of low-fluidic, ordered membrane at the nonadhered regions. Taken together, we illustrate molecular structure of adhesion signature of cancer cells: 1) high level of cholesterol accumulation supports the low-fluidic, ordered membranes at the cell periphery (Fig. 4 *F, Top*), and 2) high level of mono-/polyunsaturated lipid of the membrane provides large fluidic distribution at the nonadhered region (Fig. 4 *F, Bottom*).

Below we further discuss the 1) molecular supports for lipidomic origins of adhesion signatures of cancer cells and their role in cell migration and highlight the 2) significance of our advanced optical microscope in comparing to other studies.

Lipidomic Origins of Adhesion Signatures of Cancer Cells and Their Role in Cell Migration. Treatment with HMGCR inhibitor, lovastatin revealed that the cholesterol levels contribute to cancer-specific adhesion signature, low-fluidic, ordered membrane domains at the cell periphery. The observation that lovastatin treatment leads to the disappearance of such domains indicates the accumulation of cholesterol to the cell periphery of malignant cells (Fig. 4 *F, Top*), and our findings are supported by various previous findings on cancer cell membranes; for example, the elevation of cholesterol esters stored in human breast cancer cells (21), the spreading of MCF7 significantly suppressed by the treatment of lovastatin (22), and the accumulation of cholesterol at the spreading front of melanoma cells (23).

Furthermore, our results with SCD1 inhibitor, CAY10566, indicate that cancer-specific adhesion signature, i.e., the large deviation of the low-fluidic, ordered lipid domains at the nonadhered regions, was in relation to the levels of the mono-/polyunsaturated lipid (Fig. 4 *F, Bottom*). The large deviation indicates the lipid-compositional heterogeneity in breast cancer cell membranes. This result coincides with mass spectroscopical analysis demonstrating that unsaturated fatty acids localize to the periphery of the tumors and may increase cell membrane fluidity (24). Furthermore, He et al. reported the increased levels of monounsaturated lipids which might be associated with the malignancy of breast cancer cells (25).

Taking both inhibitor's results together, we hypothesize that 1) the high level of cholesterol and its accumulation at the cell periphery and 2) the heterogeneously distributed mono-/polyunsaturated lipids drive cell migration and cancer progression in breast cancer cells.

In recent years, it has been recognized that transcriptomic/epigenetic heterogeneity exists in cancer cell lines (26), and there is a need to evaluate this heterogeneity from multiple perspectives. Previous complementary spectroscopic studies have revealed that lipid-compositional heterogeneity (27) and the degree of lipid desaturation are present in cancer cells and cancer stem cells (28). Varieties of lipids have attracted much attention due to roles as mediators of cancer progression (29). Our data for evaluating the deviation of low-fluidic, ordered lipid domains at the nonadhered region provide an useful physical indicator to evaluate such lipid-compositional cancer heterogeneity from the physical viewpoint. We foresee that further experiments will unshed the role of such adhesion signatures in the cancer progression.

Significance of Our Advanced Optical Microscope. Our advanced optical microscope monitored "living" cell adhesion and detected low-fluidic, more ordered lipid regions at the nonadhered regions. Gaus et al. first assessed the membrane fluidity of mouse embryonic fibroblasts in adhered and nonadhered regions by combining ratiometric spectral imaging using the Laurdan probe with immunofluorescence staining of cell adhesion molecules. Their methodologies revealed that membrane regions with integrin clusters were low-fluidic (13). However, the use of surfactants for immunostaining influences membrane solubilization (30), leading to the masking of the native membrane morphology. Furthermore, the presence of integrins does not necessarily imply direct cell adhesion. For example, interferometric microscopy revealed that the tight contact region of malignant cancer cells showed a low spatial correlation with the region of high expression of the focal

complex (31). Thus, physical adhesion should be evaluated by introducing other techniques without fixation procedures. Here, our advanced optical microscopy does not need the fixation procedures due to the improvement of the optical path (Fig. 1). Thus, it enables us simultaneous visualization of membrane fluidity and morphology of living cell adhesion.

To highlight the impact of our methodologies, we first take the example of the epithelial-to-mesenchymal transition (EMT) process, one of the priming events for tumor development and trait of malignancy (21). Biological metabolic analysis has been widely used to understand metabolic reprogramming during the EMT process, and lipids are known to play as mediators of cancer progression (29). The gold standard tool to identify the cell metabolic changes is mass spectroscopy (25, 32) which cannot provide a "living" dynamical transition of cells. Raman spectroscopic imaging sensitively revealed lipid desaturation levels as metabolic markers and therapeutic targets of living ovarian cancer stem cells (28); however, such internal imaging alone does not provide insights into the dynamic cell adhesion transition during EMT. In contrast, our advanced optical microscopy can monitor the time course of dynamical biophysical changes in the metastatic cells (Fig. 3) and can be potentially applied to visualize the EMT process from the biophysical point of view.

To highlight the potential applicability of our advanced optical microscopy, we expanded to extract adhesion signatures of mouse melanoma cells with high metastatic potential (B16-F10) and low metastatic potential (B16-F1) (*SI Appendix*, Fig. S3A). Both cancer cells showed positive and negative peaks at GP of approximately –0.3 and +0.8, respectively, indicating that the low-fluidic, ordered lipid regions at the nonadhered region are common adhesion signatures for various types of cells. In addition, highly metastatic cancer cells showed a larger SD, suggesting that high-fluidic adhered membrane domains are also a common feature of cancer cells. Inhibitor experiments revealed the following molecular mechanism: The low-fluidic domains in the cell periphery were supported by cholesterol dedicated to the fluidic signature of cancer cells (Fig. 4 *G, Left*). SCD1 contributes to the synthesis of fluidic lipids, which can lead to a wide heterogeneity of cells (Fig. 4 *G, Right*). Previous complementary spectroscopic studies have revealed that lipid heterogeneity (27) and the degree of lipid desaturation are present in cancer stem cells (28). Thus, the large fluidic variation between the nonadhered and adhered regions among cells reflects the phenotypic variation in cancer cells. Interestingly, our advanced optical microscopy technique can also be a powerful tool for quantifying the response of the dose to external factors (e.g., extracellular matrix concentration; *SI Appendix*, Fig. S3B). Adding fibronectin to the substrate enhanced the fluidic deviation of highly metastatic cancer cells to a greater extent than that of low metastatic cancer cells. These results highlight the sensitivity of our microscopy technique to detect large genotypic/phenotypic variations in metastatic cancer cells using a physical approach (27). Recently, physical hallmarks of cancer cells can be considered as new targets for immunotherapy (33, 34). Nia et al. also emphasized the links between cancer biology and physics that broaden the potential discovery of drugs and treatment strategies (35). In this study, we focused on the cholesterol and unsaturated lipid synthesis pathway for cancer cells (Fig. 4). Recent progress come to focus on its corresponding drug inhibitor as a new therapeutic target for cancers (36, 37). Taken together, our advanced optical microscopy also has the potential to screen drug inhibitors from the physical point of view. Therefore, it has potential applicability to detect cell adhesion signature in a broad range of research fields, such as cancer diagnosis, drug discovery, tissue formation, and organ development.

Materials and Methods

Materials and reagents. Unless otherwise stated, all chemicals were purchased from Wako or Life Technologies (Tokyo, Japan) and used without further purification. Deionized water obtained from a Milli-Q device (Japan Millipore Ltd.) was used in this study.

Optical Setup. As schematically illustrated in Fig. 1, we used a confocal laser-scanning microscope (ECLIPSE Ti2-E, A1R MP+, Nikon Solutions, Tokyo, Japan) with an oil-immersion objective (SR HP Plan Apo 100× Sil, NA = 1.35, Nikon Solutions). A double-photon laser (femtosecond laser, λ = 780 nm, Δt ~75 fs, Chameleon, Coherent, CA) and single-photon laser (λ = 561 nm, Nikon solutions) were used as the light sources for the Laurdan probe and IRM imaging, respectively. The fluorescence signals of 6-dodecanoyl-2-dimethylaminonaphthalene (Laurdan; Thermo Fisher Scientific, Tokyo, Japan) were collected separately using GaAsP detectors (Ch1 and Ch2). A combination of dichroic mirror 1 (DM1, ZT473rdcxt, 25.5 × 36 × 1 mm, Chroma Technology, Yokohama, Japan) and a single bandpass filter (FF01-440/40-25, Semrock, IL) collected fluorescence signals in channel 1 (λ = 420 to 460 nm). A combination of dichroic mirror 2 (DM2, FF552-Di02-25 × 36, Semrock) and a single bandpass filter (FF01-494/41-25, Semrock) collected fluorescence signals in channel 1 (λ = 474 to 515 nm). The light reflected from the single-photon laser was captured using a conventional PMT detector (Ch3) passing through the DM2. IR-cut filters cut the reflected infrared light. Using this optical setup, simultaneous GP and IRM imaging with video flame rates was obtained. Analyses of membrane fluidity and topography analyses were performed using Fiji software or a custom macro in Igor PRO (analysis protocol described in *SI Appendix, Supporting Method* and Fig. S2).

Preparation of GUVs. We followed the protocol described in our previous report (38). Briefly, 1,2-dioleoyl-sn-glycerol-3-phosphocholine (DOPC, Avanti, AL) chloroform solution (5 mg/mL), and 0.02 mg/mL Laurdan chloroform solution were mixed to obtain 0.5 mol % Laurdan solution in DOPC films on an indium tin oxide (ITO) glass substrate. A spin coater (Micasa, Tokyo, Japan) was used to form lipid films at 300 rpm for 5 min. After 30 min of vacuum treatment, the glass was placed on custom-built electroforming equipment. Next, 1.2 mL of 300 mM sucrose solution (Ultra Pure, Wako) was added and an AC current was applied at 3 V and 10 Hz for 2 h using a functional generator. The GUVs were prepared by dropping 200 μL of GUV dispersion into 1 mL of 720 mM glucose solution (Wako), which was allowed to stand for 10 min. Measurement was performed by dropping 100 μL into a Chamilde chamber (Live Cell Instrument, Gyeonggi-do, Korea) chamber containing 1 mL of 720 mM glucose solution. For the aminosilylation of the glass substrate, a hydrophilic coverslip was immersed in methanol and sonicated for 5 min. The coverslip was then rinsed three times with toluene (Wako), immersed in fresh toluene, and then 0.5 or 1% (v/v) 3-aminopropyltriethoxysilane (APTES; Tokyo Kasei Kogyo) was added to the toluene and allowed to stand under cover for 15 min. Aminosilanization was performed on coverslip surfaces. The coverslips were rinsed three times with toluene and methanol, dried with nitrogen gas, and heat-treated at 110 °C for 15 min.

Cell Culture. The nonmalignant human breast cell line (MCF10A) was maintained in DMEM/F12 (11330-032, Gibco, Thermo) supplemented with the MEGM Single Quots Additive Factor Kit (cc-4136, Lonza, Basel, Switzerland) and 10% FBS (10437-028, Thermo). The human mammary carcinoma cell line (MCF7) was maintained in DMEM (11885-084, Thermo), 10% FBS (10437-028, Thermo), 1% nonessential amino acids (NEAA, 11140-050, Thermo), and 1% penicillin–streptomycin solution (168-23191, Wako, Tokyo, Japan). Mouse melanoma cell lines with low metastatic potential (B16-F1) and high metastatic potential (B16-F10) were maintained in Dulbecco's modified Eagle medium (DMEM; Nissui, Tokyo, Japan) supplemented with 10% fetal bovine serum (FBS) (SAFC Biosciences, Merck, Tokyo, Japan), 1% GlutaMAX (Thermo), 0.2% sodium bicarbonate (Thermo), and 1% penicillin–streptomycin solution (Wako, Tokyo, Japan). For simultaneous measurement of Laurdan and IRM imaging, 2×10^5 trypsinized cells were seeded on a glass bottom plate (IWAKI, Tokyo, Japan) and coated with fibronectin (Merk, Tokyo, Japan), and the Laurdan probe in DMSO solution (10 μM in final) was applied. After incubation in a 5% CO_2 incubator at 37 °C for 30 min, the cells were washed with L15 solution containing 20 mM HEPES (pH 7.4). The cells were placed in a tabletop incubator (NU8H-ZILCS-F1; TOKAI HIT, Shizuoka, Japan) at 37 °C for visualization.

For the inhibitor treatment, cells were seeded in 24-well plates. Suspensions were added to increase the cell count to 1.5×10^5 cells, and the culture medium was adjusted to 0.5 mL with the addition of lovastatin solution: 0.395 μL of 2 mM lovastatin DMSO was added to MCF10A; 0.395 μL of 10 mM lovastatin DMSO solution was added to MCF7. On days 2 and 3, the supernatant was removed, an equal volume of culture medium and lovastatin-DMSO solution was added again, and the culture was incubated at 37 °C in a 5% CO_2 environment. The cells were then trypsinized for use in cell adhesion experiments.

Author affiliations: [a]Department of Applied Physics, Graduate School of Engineering, Osaka University, Suita 565-0871, Japan; [b]Division of Precision Engineering and Applied Physics, Center for Future Innovation, Graduate School of Engineering, Osaka University, Suita, Osaka 565-0871, Japan; [c]Department of Chemistry, Saitama University, Sakura-Ku, Saitama 338-8570, Japan; [d]Division of Strategic Research and Development, Graduate School of Science and Engineering, Saitama University, Sakura-Ku, Saitama 338-8570, Japan; and [e]Directorate of Engineering, US National Science Foundation, Alexandria, VA 22314

Author contributions: T.M. and H.Y.Y. designed research; T.M., M.F., H.N., S.T., H.Y.Y., and M.W. performed research; T.M. and S.T. contributed new reagents/analytic tools; T.M., M.F., H.N., S.T., and M.W. analyzed data; and T.M., M.S., S.S., N.K., R.K., S.N., and H.Y.Y. wrote the paper.

1. D. M. Owen, C. Rentero, A. Magenau, A. Abu-Siniyeh, K. Gaus, Quantitative imaging of membrane lipid order in cells and organisms. *Nat. Protoc.* **7**, 24–35 (2011).
2. A. Abu-Siniyeh *et al.*, The aPKC/Par3/Par6 polarity complex and membrane order are functionally interdependent in epithelia during vertebrate organogenesis. *Traffic* **17**, 66–79 (2016).
3. K. Yamamoto, J. Ando, Vascular endothelial cell membranes differentiate between stretch and shear stress through transitions in their lipid phases. *Am. J. Physiol. Heart Circ. Physiol.* **309**, H1178–H1185 (2015).
4. K. Yamamoto, Y. Nogimori, H. Imamura, J. Ando, Shear stress activates mitochondrial oxidative phosphorylation by reducing plasma membrane cholesterol in vascular endothelial cells. *Proc. Natl. Acad. Sci. U.S.A.* **117**, 33660–33667 (2020).
5. C. Angelucci *et al.*, Epithelial-stromal interactions in human breast cancer: Effects on adhesion, plasma membrane fluidity and migration speed and directness. *PLoS One* **7**, e50804 (2012).
6. G. L. Nicolson, Cell membrane fluid-mosaic structure and cancer metastasis. *Cancer Res.* **75**, 1169–1176 (2015).
7. M. Sok, M. Sentjurc, M. Schara, Membrane fluidity characteristics of human lung cancer. *Cancer Lett.* **139**, 215–220 (1999).
8. W. Zhao *et al.*, Candidate antimetastasis drugs suppress the metastatic capacity of breast cancer cells by reducing membrane fluidity. *Cancer Res.* **76**, 2037–2049 (2016).
9. J. T. Parsons, A. R. Horwitz, M. A. Schwartz, Cell adhesion: Integrating cytoskeletal dynamics and cellular tension. *Nat. Rev. Mol. Cell Biol.* **11**, 633–643 (2010).
10. B. Schaeffer, A. Curtis, Effects on cell adhesion and membrane fluidity of changes in plasmalemmal lipids in mouse L929 cells. *J. Cell Sci.* **26**, 47–55 (1977).
11. K. Salaita *et al.*, Restriction of receptor movement alters cellular response: Physical force sensing by EphA2. *Science* **327**, 1380–1385 (2010).
12. C. Eich *et al.*, Changes in membrane sphingolipid composition modulate dynamics and adhesion of integrin nanoclusters. *Sci. Rep.* **6**, 20693 (2016).
13. K. Gaus, S. Le Lay, N. Balasubramanian, M. A. Schwartz, Integrin-mediated adhesion regulates membrane order. *J. Cell Biol.* **174**, 725–734 (2006).
14. E. Sackmann, R. F. Bruinsma, Cell adhesion as wetting transition? *Chemphyschem* **3**, 262–269 (2002).
15. T. Parasassi, G. De Stasio, G. Ravagnan, R. Rusch, E. Gratton, Quantitation of lipid phases in phospholipid vesicles by the generalized polarization of Laurdan fluorescence. *Biophys. J.* **60**, 179–189 (1991).
16. K. Gaus *et al.*, Visualizing lipid structure and raft domains in living cells with two-photon microscopy. *Proc. Natl. Acad. Sci. U.S.A.* **100**, 15554–15559 (2003).
17. L. Limozin, K. Sengupta, Quantitative reflection interference contrast microscopy (RICM) in soft matter and cell adhesion. *Chemphyschem* **10**, 2752–2768 (2009).

18. T. Matsuzaki *et al.*, High contrast visualization of cell–hydrogel contact by advanced interferometric optical microscopy. *J. Phys. Chem. Lett.* **5**, 253–257 (2014).

19. O. Bjarnadottir *et al.*, Statin use, HMGCR expression, and breast cancer survival–The Malmo diet and cancer study. *Sci. Rep.* **10**, 558 (2020).

20. C. Angelucci *et al.*, Pivotal role of human stearoyl-CoA desaturases (SCD1 and 5) in breast cancer progression: Oleic acid-based effect of SCD1 on cell migration and a novel pro-cell survival role for SCD5. *Oncotarget* **9**, 24364 (2018).

21. A. Morandi, M. L. Taddei, P. Chiarugi, E. Giannoni, Targeting the metabolic reprogramming that controls epithelial-to-mesenchymal transition in aggressive tumors. *Front. Oncol.* **7**, 40 (2017).

22. R. Abolghasemi, S. Ebrahimi-Barough, N. Bahrami, J. Aid, Atorvastatin inhibits viability and migration of MCF7 breast cancer cells. *APJCP* **23**, 867 (2022).

23. J. Bi, R. Wang, X. Zeng, Lipid rafts regulate the lamellipodia formation of melanoma A375 cells via actin cytoskeleton-mediated recruitment of β1 and β3 integrin. *Oncol. Lett.* **16**, 6540–6546 (2018).

24. T. B. Angerer, Y. Magnusson, G. R. Landberg, J. S. Fletcher, Lipid heterogeneity resulting from fatty acid processing in the human breast cancer microenvironment identified by GCIB-ToF-SIMS imaging. *Anal. Chem.* **88**, 11946–11954 (2016).

25. M. He, S. Guo, Z. Li, In situ characterizing membrane lipid phenotype of breast cancer cells using mass spectrometry profiling. *Sci. Rep.* **5**, 11298 (2015).

26. Q. Zhu *et al.*, Single cell multi-omics reveal intra-cell-line heterogeneity across human cancer cell lines. *Nat. Commun.* **14**, 8170 (2023).

27. T. B. Angerer, Y. Magnusson, G. Landberg, J. S. Fletcher, Lipid heterogeneity resulting from fatty acid processing in the human breast cancer microenvironment identified by GCIB-ToF-SIMS imaging. *Anal. Chem.* **88**, 11946–11954 (2016).

28. J. Li *et al.*, Lipid desaturation is a metabolic marker and therapeutic target of ovarian cancer stem cells. *Cell Stem. Cell* **20**, 303–314.e5 (2017).

29. F. C. Vogel, A. B. Chaves-Filho, A. Schulze, Lipids as mediators of cancer progression and metastasis. *Nat. Cancer* **5**, 16–29 (2024).

30. M. Jones, Surfactants in membrane solubilisation. *Int. J. Pharm.* **177**, 137–159 (1999).

31. T. Matsuzaki *et al.*, Quantitative evaluation of cancer cell adhesion to self-assembled monolayer-patterned substrates by reflection interference contrast microscopy. *J. Phys. Chem. B* **120**, 1221–1227 (2016).

32. N. Vidavsky *et al.*, Mapping and profiling lipid distribution in a 3D model of breast cancer progression. *ACS Central Sci.* **5**, 768–780 (2019).

33. H. Guo, T. Zhang, Y. Yu, F. Xu, Cancer physical hallmarks as new targets for improved immunotherapy. *Trends Cell Biol.* **31**, 520–524 (2021).

34. D. Vanauberg, C. Schulz, T. Lefebvre, Involvement of the pro-oncogenic enzyme fatty acid synthase in the hallmarks of cancer: A promising target in anti-cancer therapies. *Oncogenesis* **12**, 16 (2023).

35. H. T. Nia, L. L. Munn, R. K. Jain, Physical traits of cancer. *Science* **370**, eaaz0868 (2020).

36. Z. Tracz-Gaszewska, P. Dobrzyn, Stearoyl-CoA desaturase 1 as a therapeutic target for the treatment of cancer. *Cancers* **11**, 948 (2019).

37. C. Liu *et al.*, New insights into the therapeutic potentials of statins in cancer. *Front. Pharm.* **14**, 1188926 (2023).

38. T. Matsuzaki *et al.*, Adsorption of galloyl catechin aggregates significantly modulates membrane mechanics in the absence of biochemical cues. *Phys. Chem. Chem. Phys.* **19**, 19937–19947 (2017).